Research in Astronomy and Astrophysics, 23:085005 (14pp), 2023 August https://doi.org/10.1088/1674-4527/acd89f

Does Diffuse Circumnuclear Gas around Sgr A* Achieve Collisional Ionization Equilibrium or Remain Non-equilibrium Ionization?

Shu Niu[1,2], Fu-Guo Xie[1], Wei Sun[3,4], and Li Ji[3,4]
[1] Key Laboratory for Research in Galaxies and Cosmology, Shanghai Astronomical Observatory, Chinese Academy of Sciences, Shanghai 200030, China
niushu@pmo.ac.cn, fgxie@shao.ac.cn
[2] University of Chinese Academy of Sciences, Beijing 100049, China
[3] Purple Mountain Observatory, Chinese Academy of Sciences, Nanjing 210023, China; ji@pmo.ac.cn
[4] Key Laboratory of Dark Matter and Space Astronomy, Chinese Academy of Sciences, Nanjing 210023, China
Received 2023 April 13; revised 2023 May 5; accepted 2023 May 16; published 2023 July 5

Abstract

The feeding and feedback processes at the vicinity of a supermassive black hole (BH) are essential for our understanding of the connection between supermassive BH and its host galaxy. In this work, we provide a detailed investigation, both observational and theoretical, on the diffuse (∼2″–20″, ∼0.08–0.8 pc) X-ray emission around Sgr A*. Over two-decade Chandra observations are gathered to obtain highest signal-to-noise to date. We find that, the line center of iron lines of the outer 8″–18″ region, $\epsilon_c = 6.65^{+0.02}_{-0.03}$ keV, is comparable to that ($\epsilon_c = 6.60^{+0.05}_{-0.03}$ keV) of the inner 2″–5″ region. This is somewhat unexpected, since the gas temperature decreases further away from the central BH. Based on a dynamical inflow–outflow model that considers the gas feeding by stellar winds from Wolf–Rayet stars, we calculate the X-ray spectrum based on both the conventional collisional ionization equilibrium (CIE) assumption, and the newly developed non-equilibrium ionization (NEI) assumption. We find that, theoretically gases within ∼8″–10″ remain in a CIE state, outside of this radius they will be in the NEI state. A comparison of the properties of ∼6.6 keV iron lines between CIE and NEI is addressed. Interestingly, the NEI interpretation of outer region is supported by the Chandra line center ϵ_c measurements of this region.

Key words: X-rays: diffuse background – galaxies: active – Galaxy: center – (galaxies:) quasars: emission lines

1. Introduction

Sgr A*, at the center of the Milky Way, is the closest supermassive black hole (BH). It is at a distance of $d = 8.13$ kpc and has a BH mass of $M_{\rm BH} = 4.14 \times 10^6 M_\odot$ (both are mean of values reported in Do et al. 2019 and Gravity Collaboration et al. 2019, which differ from each other by $\lesssim$4%).[5] The spectrum of Sgr A* peaks at the submillimeter wave band (Bower et al. 2019), and its bolometric luminosity is constrained to be $L_{\rm bol} \approx 6.9 \times 10^{35}$ erg s^{-1} (Bower et al. 2019; Wielgus et al. 2022; Xie et al. 2023), or equivalently the Eddington ratio $\lambda_{\rm Edd} \equiv L_{\rm bol}/L_{\rm Edd} \approx 1.5 \times 10^{-9}$. Here the Eddington luminosity for accretion onto a $M_{\rm BH}$ mass of a BH is $L_{\rm Edd} = 4\pi Gcm_p M_{\rm BH}/\sigma_T = 1.26 \times 10^{44}(M_{\rm BH}/10^6 M_\odot)$ erg s^{-1}. Such low $\lambda_{\rm Edd}$ is probably caused by two reasons. First, the accretion rate at the influence radius of a BH, so-called the Bondi radius,[6] is sufficiently low (Baganoff et al. 2003; Wang et al. 2013), $R_{\rm Bondi} \approx 1''$. From linear polarization observations in millimeter radio, the accretion rate near BH horizon is found to be even lower (e.g., Aitken et al. 2000; Bower et al. 2003; Marrone et al. 2006), suggesting the existence of strong outflow (Yuan et al. 2003; Roberts et al. 2017). Second, the radiative efficiency of accretion in Sgr A* is in the range 0.1%–0.2% (Xie et al. 2023), which is much lower than the typical 10% of cold accretion disk (Shakura & Sunyaev 1973).

The basic properties of Sgr A* have been successfully interpreted under the hot accretion flow model (and its several variations; Narayan et al. 1995; Yuan et al. 2003; Genzel et al. 2010; Event Horizon Telescope Collaboration et al. 2022). This model assumes that the accreting gas is hot, with gas temperature near the viral value at each radius. In this case, the system is expected to be geometrically thick but optically thin (Yuan & Narayan 2014). Recently, the Event Horizon Telescope has advanced our understanding of Sgr A* and its accretion physics, where not only the optical-thin nature in sub-mm bands but also the low radiative efficiency are now confirmed (Event Horizon Telescope Collaboration et al. 2022). The dominant radiation process is synchrotron emission for the sub-mm bump (Yuan et al. 2003; Bower et al. 2019; Wielgus et al. 2022), and bremsstrahlung emission of hot gas near the Bondi radius for the X-rays in quiescent state

[5] In this work, three length units are used equally, i.e., arc second ″, parsec pc, and gravitational radius of BH $R_g(\equiv GM_{\rm BH}/c^2)$. For our chosen BH mass and distance, we have $1'' \approx 3.94 \times 10^{-2}$ pc $\approx 2.00 \times 10^5 R_g$.

[6] $R_{\rm Bondi} \approx 0.155 \times (T_{\rm gas}/10^7\,{\rm K})^{-1}$ pc $\approx 3\rlap{.}''95 \times (T_{\rm gas}/10^7\,{\rm K})^{-1}$, where from spectral modeling the gas temperature is constrained to be $T_{\rm gas} \approx 1.9$ keV $\approx 4 \times 10^7$ K (Baganoff et al. 2003).

Table 1
Summary and OBSIDs of Chandra Observations of Sgr A*

Type/Mode	ACIS	HETG	Obs. Period	Raw Data[a]		Final Data[b]	
				OBSID Counts	Exposure (Ms)	OBSID Counts	Exposure (Ms)
ChI	ACIS-I	NO	1999-09 to 2013-04	48	1.5	48	1.39
	242 1561 2951 2952 2953 2954 2943 3663 3392 3393 3665 3549 4683 4684 5360 6113 5950 5951 5952 5953 5954 6639 6640 6641 6642 6363 6643 6644 6645 6646 7554 7555 7556 7557 7558 7559 9169 9170 9171 9172 9174 9173 10556 11843 13016 13017 14941 14942						
ChH	ACIS-S	YES	2012-06 to 2013-06	41	3.0	41	2.81
	13850 14392 14394 14393 13856 13857 13854 14413 13855 14414 13847 14427 13848 13849 13846 14438 13845 14460 13844 14461 13853 13841 14465 14466 13842 13839 13840 14432 13838 13852 14439 14462 14463 13851 15568 13843 15570 14468 15040 15651 15654						
ChS	ACIS-S	NO	2013-05 to 2019-08	53	1.8	10	0.49
	14702 14703 14946 15041 15042 14945 15043 14944 15044 14943 14704 15045 16508 16211 16212 16213 16214 16210 16597 16215 16216 16217 16218 16963 16966 16965 16964 18055 18056 18731 18732 18057 18058 19726 19727 20041 20040 19703 19704 20344 20345 20346 20347 21453 21454 21455 21456 22230 20446 20447 20750 22288 20751						

Notes. The OBSIDs, sorted by date, are listed in the Table. Underlines mark those that are excluded from our analysis of diffuse X-ray emission.
[a] The count and exposure time are for the parent sample (by early 2021).
[b] The count and exposure time are for the final sample, i.e., after removing flaring intervals and bright contamination sources, see Section 2 for details.

(Quataert 2002; Yuan et al. 2003; Quataert 2004; Wang et al. 2013; Corrales et al. 2020; see Section 2.3 below for X-rays in the flare state). Indeed, the hot accretion flow model can nicely reproduce the spectral energy distribution of Sgr A* in quiescence (Yuan et al. 2003; Ma et al. 2019).

The diffuse hot gas around Sgr A* is found to extend from sub-Bondi up to pc scales (equivalently, from sub-arcseconds up to several arcminutes, Baganoff et al. 2003; Muno et al. 2004). In this work, we primarily focus on those hot "circum-nuclear" gases from regions outside of the Bondi radius.[7] This region is important in two aspects (Genzel et al. 2010), it not only provides the feeding condition of accretion, but also directly reflects the feedback of nuclear BH activities and stellar processes (supernovae, stellar wind) in this region. Indeed, the diffuse soft X-rays at scales larger than $\sim 1'$ are quite asymmetric and show filamentary features in soft X-rays, compared to the more uniform distribution in hard X-rays (Muno et al. 2004). They may be created by collisions of stellar winds and/or the expanding supernova remnants (e.g., Zhang et al. 2023, see Genzel et al. 2010 for a review). Quataert (2004, see also Xu et al. 2006) is pioneered in understanding the gas properties between $\sim 0\farcs2$ and $\lesssim 10''$. In their models, they consider Sgr A* is fed by stellar winds in circum-nuclear regions, and agreements to current BH activities are found (Shcherbakov & Baganoff 2010, for numerical simulations see e.g., Cuadra et al. 2006; Ressler et al. 2020, 2023).

[7] Note that $2''$–$5''$, and $6''$–$20''$ regions are called Sgr A*-halo and off-halo respectively, in Wang et al. (2013). A possible arc-shaped feature between $10''$ and $15''$ is coined as "X-ray ridge" (Rockefeller et al. 2005). In this work, we are mostly interested in the off-halo region.

In this work, we follow Xu et al. (2006) and Shcherbakov & Baganoff (2010), with several updates. First, we extend to include a larger region of up to $\sim 20''$ (i.e., up to sub-pc scale), which now has sufficient signal-to-noise thanks to the continuous efforts of Chandra. As we will show in Section 3.2.1, such extension is necessary for our investigation of non-equilibrium ionization process (NEI, see Section 3.2 below, and Ji et al. 2006; Zhang et al. 2023). Second, also the motivation of this work is to probe the possible observational evidence of NEI in Sgr A*. Most previous work, including Quataert (2004) and Xu et al. (2006), assumed a collisional ionization equilibrium (CIE) for their spectral line calculations. However, whether or not CIE can be achieved needs to be examined. Third, the atomic database `AtomDB` has also undergone a number of updates and supplements. Since version 3.0, `AtomDB` has included data and model to consider the NEI effect (Foster et al. 2017).

This work is organized as follows. In Section 2 we provide our data selection and reduction. Because the spatial resolution is of crucial importance for our investigation, we only consider Chandra data. Section 3 is devoted to detailed descriptions of our model, i.e., the inflow–outflow model for the dynamical structure (see Section 3.1), and the non-equilibrium ionization model for the radiation (see Section 3.2). Our results are shown in Section 4. We finally provide a brief summary in Section 5. Throughout this work, we fix the metal abundance to 1.5, a value constrained by modeling the X-ray emission from inside the Bondi radius (Wang et al. 2013; Corrales et al. 2020).

2. Observations and Data Reduction

Table 1 summarizes the basic information of our Chandra data of Sgr A*. In this table, we include the instruments and

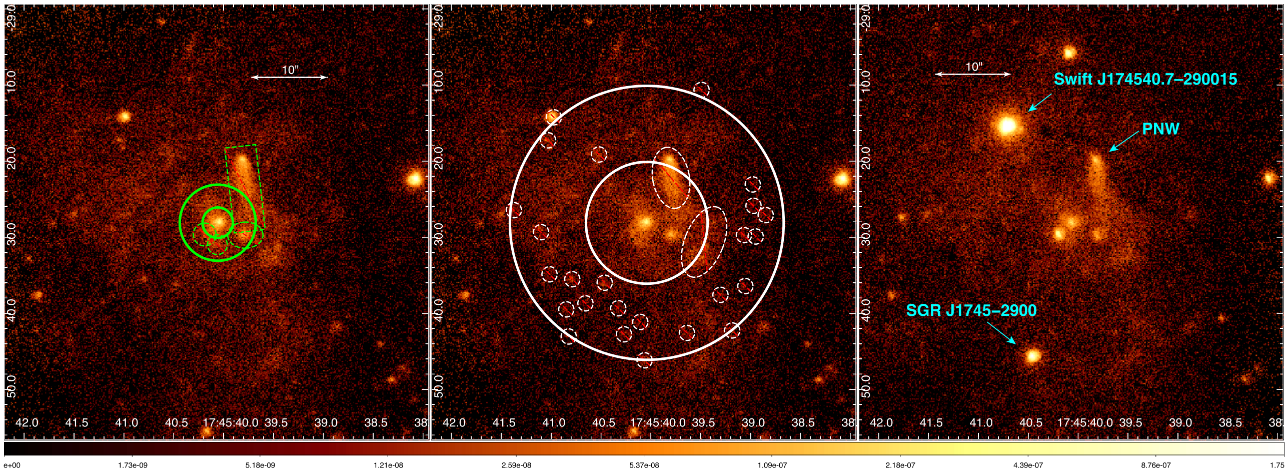

Figure 1. The combined 0.5–7 keV X-ray images of Sgr A* and its ambient region in three instrument modes, i.e., Left Panel for ACIS-I (ChI data), Middle Panel for the zeroth order image of HETG (ChH data), and Right Panel for ACIS-S (ChS data). The size of each panel is about 1′. The green and white curves in the left and middle panels indicate the boundary of two diffuse emission regions analyzed in this work, i.e., 2″–5″ for the green curves and 8″–18″ for the white ones. These two regions are plotted separately in two panels, for clarity purpose. The dashed circles mark those excluded regions that suffer contamination from point sources, e.g., PNW (see also the mark in the right panel), stars. Two bright transients, i.e., Swift J174540.7-290015 and SGR J1745-2900, are marked in the right panel.

observational period of each observational mode, and OBSID of each observation. We also provide the exposure time of the raw data and the final data after data reduction. Below are the details of our data compilation and reduction.

2.1. Parent Chandra X-Ray Data and Diffuse Region around Sgr A*

Sgr A* and its surrounding regions are undoubtedly one of the most observed at all wavelengths. Because of the complicated structure in the nuclear regions near Sgr A*, and we are interested in the circum-nuclear diffuse X-ray emission, we limit ourselves to Chandra observations, which to date has the highest X-ray spatial resolution. Moreover, because the diffuse emission can easily be affected by the core of Sgr A*, we only select observations of Sgr A* on the optical axis, i.e., off-axis angle $\lesssim 1'$. As of early 2021, Chandra has published a total of 141 observations using Advanced CCD Imaging Spectrometer (ACIS) CCD detector, with exposure time varying from 5 to 190 ks. These observations can be divided into three categories according to their observation mode. As listed in Table 1, below we provide a brief description of these observations. We also show in Figure 1 the combined 0.5–7 keV X-ray images of Sgr A* and its ambient region.

1. 48 ChI observations. There are 46 observations before 2012 and additional two in 2013 (OBSIDs 14 941 and 14 942) that used the front-illuminated (FI) CCD ACIS-I as the backend detector (i.e., ChI stands for Chandra/ACIS-I). Using the Full Frame mode, the temporal resolution is about 3.2 s. The accumulated total exposure time of all the ChI observations is about 1.5 Ms. The left panel of Figure 1 shows a combined flux image in this mode.
2. 41 ChH observations. The 38 observations of the Chandra Galactic Center X-ray Visionary Program (GCXVP[8]) project in 2012, and additional three in 2013 (OBSIDs 15 040, 15 651, and 15 654) used the HETG and the back-illuminated (BI) ACIS-S CCD (ChH for Chandra/HETG) with a time resolution of about 3.2 s. However, due to the spectral effect of the grating, for the zeroth order grating data that we analyze for the diffuse radiation, the effective area is about half to that of other modes. The accumulated total exposure time is about 3.0 Ms. The middle panel of Figure 1 shows the combined flux image.
3. 53 ChS observations. The remaining 53 observations since 2013 only use ACIS-S as the backend detector (ChS for Chandra/ACIS-S). Here 1/8 subarray mode is used, therefore, the time resolution is increased to 0.7 s. The accumulated total exposure time is about 1.8 Ms. The right panel of Figure 1 shows a combined flux image in this mode.

Though energy resolution of Chandra BI CCDs is reported to be slightly better than that of FI CCDs due to less charge transfer inefficiency (CTI), we find the difference to be only ∼1.5 times for on-axis source in 2012.[9] Besides, the effect of CTI increases with time, both FI and BI energy resolutions degrade simultaneously. Moreover, nearly all the ACIS-I/FI

[8] https://space.mit.edu/CXC/SGRA/Project_Page.html
[9] The Chandra Proposers' Observatory Guide, https://cxc.cfa.harvard.edu/proposer/POG/.

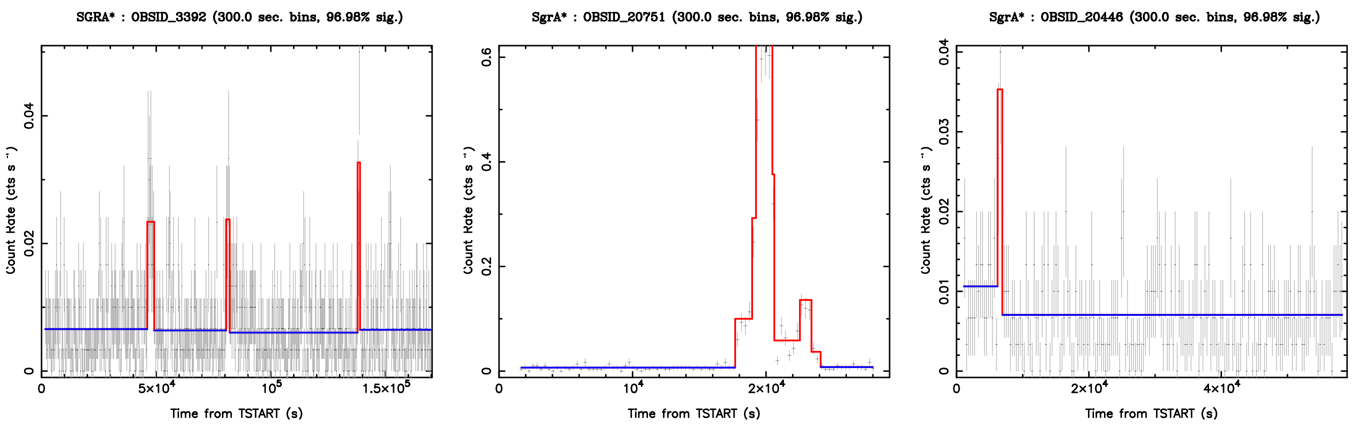

Figure 2. Examples of flare detection by the Bayesian block algorithm. The gray points represent the light curve of the Sgr A* core (defined as within 1$''$.5). The red and the blue intervals mark, respectively, the detected flares and the quiescent non-flare state. The confidence level of the count rate change is 96.98%. Panels from left to right are from observations of mode, ChI, ChH, and ChS. OBSID of each observation is also labeled in each panel.

observations in this work were taken before 2012, which on average are much earlier than the first ACIS-S/BI observation (in 2012). Thus we believe the line resolution varies slightly among different instrumental modes. We additionally note that since we are interested in diffuse X-ray emission around Sgr A*, we neglect all the minor differences in spatial resolution among the three modes.

For our motivation, we select two regions of diffuse emission for comparison. The inner one is 2$''$–5$''$ annulus, whose boundaries are shown by green solid curves in the left panel of Figure 1. This is only outside of the Bondi radius of Sgr A*, the feeding zone of nuclei activity. The outer one is 8$''$–18$''$ annulus, whose boundaries are shown by white solid curves in the middle panel of Figure 1. This more extended region represents gas that locates further distant away and suffer impacts of circumnuclear stellar activities. The background is extracted from the nearby 21$''$–30$''$ annulus and its contribution is subtracted.

2.2. Exclude Impact of Outbursts of Nearby Point Sources

We notice that outbursts are observed in both Magnetar SGR J1745-2900 (located at a distance of 2$''$.4 from Sgr A*, Kaspi et al. 2014; Coti Zelati et al. 2017) and the low-mass X-ray binary Swift J174540.7-290015 (16$''$ from Sgr A*, Ponti et al. 2016; Corrales et al. 2017). Because of the faintness of Sgr A* ($\sim 2 \times 10^{33}$ erg s^{-1} in X-rays, Baganoff et al. 2003), the luminosity of the magnetar at early flare stage is two orders of magnitude brighter than Sgr A* in quiescence, and the X-ray binary can be four orders of magnitude brighter than that of Sgr A*. In this situation, the dust scattering effect (Smith & Dwek 1998; Smith et al. 2016) from these two transients will significantly complicate our analysis of diffuse emission around Sgr A*.

In order to constrain their contamination, we rely on long-term monitoring of these two transients. Clearly after the outburst, the light curve of these two transients decreases gradually over time (Ponti et al. 2016; Rea et al. 2020). Through a detailed modeling of these two transients, we found that, among the 53 ChS observations, only 10 observations after 2019 are suitable for our investigation.[10] The total exposure time of all the remaining 10 ChS observations is about 0.5 Ms.

As shown in the middle panel of Figure 1, the areas circled by red dotted circle mark the location of contaminated point sources, taken from the deep-field catalog of Zhu et al. (2018). These regions are also excluded from our analysis.

2.3. Exclude Data when Sgr A* is in the Flare State

Sgr A* is known to undergo numerous flares, which are most prominent in infrared and X-rays (Bower et al. 2003; Neilsen et al. 2013; Yuan & Wang 2016; Zhang et al. 2017; Haggard et al. 2019). The flares occur about once a day in X-rays. Each flare lasts from half an hour to several hours (Ponti et al. 2015; Yuan & Wang 2016; Mossoux et al. 2020). In addition, the power-law spectrum of the flare state is distinct to the quasi-thermal (bremsstrahlung) of the quiescent state (Neilsen et al. 2013; Zhang et al. 2017; Haggard et al. 2019).

During the flare state, emission from Sgr A* can spread to the surrounding medium because of the large point-spread function of the core. In order to obtain the quiescent good time intervals (GTIs, shown by blue lines in Figure 2), we use the Bayesian block method (Scargle 1998; Scargle et al. 2013) for screening. The Bayesian block algorithm creates a piecewise constant-rate light curve by taking into account each event and

[10] The 0.3–10 keV luminosity of SGR J1745-2900 after 2019 is about 4×10^{33} erg s^{-1} (Rea et al. 2020), similar to that of Sgr A* in quiescence. Swift J174540.7-290015 has a faster decay and becomes fainter than the magnetar after 2017.

its time in one observation, i.e., the light curve is represented as a series of contiguous "blocks," where the event rate is modeled as a constant. Boundaries between blocks and the rates within each block are determined by Bayesian analysis (assuming Poisson statistics). This algorithm is frequently adopted to detect flares in Sgr A* (Ponti et al. 2015; Yuan & Wang 2016; Haggard et al. 2019; Mossoux et al. 2020).

In the data analysis process, we screened the event lists of 2–8 keV within 1.″5 of Sgr A*, and passed the SITAR[11] package for screening, the selected block prior probability (which is equivalent to the presence of count rate changes) is 96.98%, and the corresponding prior block number *ncp_prior* = 3.5. We show three examples in Figure 2. The red and the blue intervals mark, respectively, the flare state and the non-flare state.

From the GTIs obtained by the Bayesian block algorithm, we then screened and extracted the spectrum of the diffuse emission when the core is in the quiescent non-flare state.

2.4. Final Chandra Data

After taking all the processes above, we come out the "cleaned" data for our investigation of the diffuse X-ray emission around Sgr A*. As listed in Table 1, the exposure time of this final selected/edited data is reduced to ≈4.9 Ms, or more specifically, 1.39 Ms for ChI, 2.81 Ms for ChH, and 0.49 Ms for ChS.

2.4.1. Spectral Modeling of Diffuse Emission under CIE Assumption

Before introducing our NEI model, we first limit ourselves to the CIE assumption (as the case of all previous work. `APEC`, Smith et al. 2001), and performed a simple analysis of the extracted spectra. We combine each spectral data set of the three instrument modes (i.e., ChI, ChH, and ChS) and do a simultaneous joint fitting in ISIS[12] software (Houck & Denicola 2000). We consider both the neutral element absorption (`TBabs`, Wilms et al. 2000) and the dust scattering (`xscat`, Smith et al. 2016), i.e., we take the model `TBabs`×`xscat`×`apec`. The metal abundance was fixed at 1.5.

The spectrum is shown in Figure 3. The left panel is for the inner region (2″–5″) of the diffuse gas, while the right panel is for the outer region (8″–18″). The χ^2/d.o.f of the former (latter) is 658.6/528 (1911.6/608). Emission from the inner region is found to be close to a CIE state, although clear deviation to the CIE model at above 6 keV can still be observed. Such deviation may suggest that the iron element does not reach a CIE state (see also Hua et al. (2023)). The difference in residuals between them is a possible indicator that the elements diverge CIE state more in the outer. The temperature of the inner region gas in this simple assumption is $1.173^{+0.032}_{-0.028}$ keV (uncertainties here and below are at 90% confidence level). As shown in small windows in Figure 3, the line center and equivalent width of the iron emission line near 6.67 keV as measured under the `powerlaw + Gaussian` model are respectively, $\epsilon_c = 6.60^{+0.05}_{-0.03}$ keV and EW = $279.5^{+206.5}_{-134.4}$ eV, consistent with Wang et al. (2013).

For the emission of the outer region, we first note that, because the total exposure time reaches 4.7 Ms, a signal-to-noise ratio of the spectrum is now improved by a factor of ∼4 compared to those adopted in previous investigations (Baganoff et al. 2003; Xu et al. 2006). Interestingly, deviations from our adopted model above are observed at several energy bands, and are most significant at the high energy part. When we compare the inner and the outer regions, we find that, more deviations to the CIE model is observed in the outer region. Considering the strong deviation to CIE model, we omit to report the derived gas temperature of the outer region. Further refinements to the CIE model are necessary.

On the other hand, the emission line of iron of the outer region can still be fit fairly well under the `powerlaw + Gaussian` model. The line center and equivalent width are respectively, $\epsilon_c = 6.65^{+0.02}_{-0.03}$ keV and EW = $293.4^{+149.6}_{-149.6}$ eV.

3. Basic Model for the Diffuse Gas around Sgr A*

3.1. Dynamical Inflow–Outflow Model

Because of the faintness of Sgr A* (i.e., $\lambda_{\rm Edd} \sim 10^{-9}$, Bower et al. 2003, 2019; Wielgus et al. 2022; Xie et al. 2023), strong winds expelled from massive Wolf–Rayet and blue giant stars within the central ∼1 pc can provide sufficient gas to feed the BH activity of Sgr A* (e.g., Cuadra et al. 2006, 2008; Martins et al. 2007, but see Lützgendorf et al. 2016). Moreover, the interaction of multiple stellar winds leads to shocks, which will heat the gas up to $kT_e \sim$ keV. The mass accretion rate near the Bondi radius reaches $10^{-3}\,M_\odot\,{\rm yr}^{-1}$. More importantly, numerical simulations have provided a self-consistent description of gas dynamics and radiation of a broad region between ∼1″ and ∼10″ (Cuadra et al. 2008; Shcherbakov & Baganoff 2010; Ressler et al. 2018, 2020).

For the reasons below, in this work we follow the one-dimensional (1D, spherically symmetric) numerical calculations of Shcherbakov & Baganoff (2010). First, as reported in Ressler et al. (2018), as long as we are interested in regions distant away from individual massive Wolf–Rayet star, the physical properties of gas determined by 3D numerical simulations agree well with those based on 1D numerical calculations. The closest star to Sgr A* (pericenter is approximately 3000 R_g), S2, is a B-type star, whose wind loss rate is about three orders of magnitude smaller than that of Wolf–Rayet stars (Shcherbakov & Baganoff 2010). Consequently, the asymmetry of the gas within ∼0.01 pc can then be safely neglected (Ressler et al. 2018). Besides, as shown in the

[11] https://space.mit.edu/cxc/analysis/SITAR/
[12] https://space.mit.edu/cxc/isis/

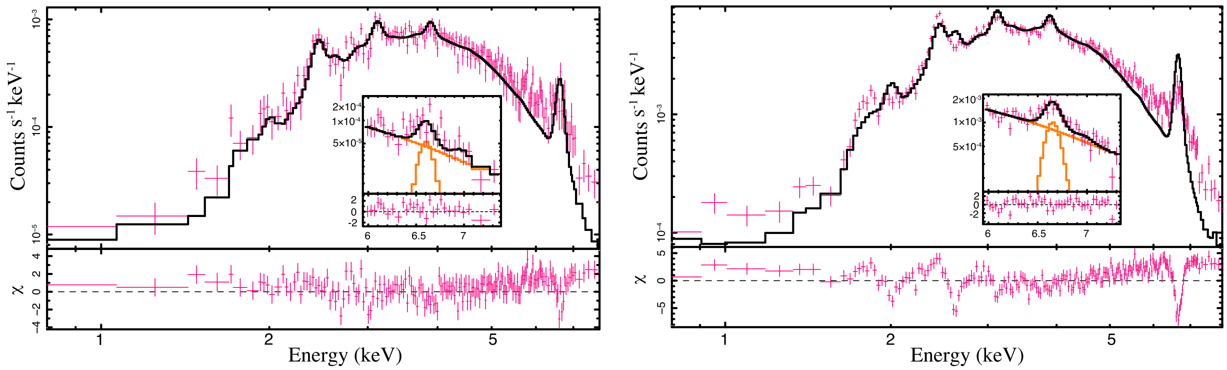

Figure 3. Spectra of diffuse emission of the inner 2″–5″ (left panel) and outer 8″–18″ (right panel) regions, based on a combined fit of all the three instrument modes, the data and model are weight-added based on exposure times and effective areas for plotting with visual clarify. The black line represents a model assuming the whole system is a single-temperature plasma and holds the CIE condition: `TBabs` × `xscat` × `apec`, where `xscat` is the model of dust scattering. The small window in each panel shows the energy range used to fit the iron emission lines by `powerlaw` + Gaussian model, where components are displayed by orange lines.

middle and right panels of Figure 1, the diffuse X-ray emission between 1″ and 20″ are fairly smooth and symmetric, suggesting that there are no strong stellar activities recently (either X-ray binaries or supernovae, but see, e.g., Zhang et al. 2023 for shocks driven by supernovae in the outer region). Second, the 1D model can reach a dynamical range in a radius of 6–7 orders of magnitude, while numerical simulations can only reach a factor of $\sim 10^{3-4}$. For simplicity, we further assume the magnetic field outside of the Bondi radius is weak. We take the stellar winds as source terms of mass, momentum, and energy in the hydrodynamic equations of the hot diffuse plasma. For our 1D, spherical symmetric mode, the dynamical equations can then be expressed as (e.g., Quataert 2004; Shcherbakov & Baganoff 2010):

$$\frac{\partial \rho}{\partial t} + \frac{1}{r^2}\frac{\partial (r^2 \rho \boldsymbol{v})}{\partial r} = q_{\rm w}(r), \tag{1}$$

$$\rho \frac{d\boldsymbol{v}}{dt} + \frac{\partial p}{\partial r} + \rho \frac{G M_{\rm tot}(r)}{r^2} = -q_{\rm w}(r)\boldsymbol{v}, \tag{2}$$

$$\rho T \frac{ds}{dt} = q_{\rm w}(r)\left[\frac{\boldsymbol{v}^2 + \langle \boldsymbol{v}_{\rm w}^2 \rangle}{2} - \frac{\gamma}{\gamma - 1} c_s^2\right] - q^{\rm rad}. \tag{3}$$

Here ρ, p, c_s, $\boldsymbol{v}$, s are respectively, the density, pressure, sound speed, radial velocity, and specific entropy of the diffuse gas. $q^{\rm rad}$ is the radiative cooling rate. $M_{\rm tot}$ represents the total mass within radius r, and we approximate it as $M_{\rm tot}(r) \approx M_{\rm BH}$. The stellar wind injection rate $q_{\rm w}$ and wind velocity $\boldsymbol{v}_{\rm w}$ take elaborated forms of Shcherbakov & Baganoff (2010, between 0.″1 and 20″, see their Figure 3), where a steady-state orbit-averaged prescription of stellar wind feeding is adopted. The total mass injection rate can then be derived as $\dot{M}_{\rm w} = \int 4\pi r^2 q_{\rm w} dr$.

Figure 4 shows the basic gas properties (left panel: number density, middle: gas temperature, and right: radial velocity) of our 1D model solution for the diffuse circum-nuclear region of Sgr A*. As shown in this figure, the stagnation point that separates inflow and outflow (Shcherbakov & Baganoff 2010) locates at $R_{\rm st} \approx 0.14$ pc.

Since the gas temperature explored in this work is relatively low, electron-ion interaction is primarily through Coulomb collisions, which takes the following relation:

$$\frac{d(T_e/T)}{dt} = 1.2 \times 10^{-4}\ {\rm yr}^{-1}\, n \left(\frac{T}{10^7\ {\rm K}}\right)^{-3/2} \times \left(\frac{T_e}{T}\right)^{-3/2}\left(1 - \frac{T_e}{T}\right), \tag{4}$$

where T_e and T correspond to temperatures of electrons and gas in general. $n \approx \rho/m_p$ (in unit of cm^{-3}) is the number density (Spitzer 1978; Borkowski et al. 1994). Clearly from this equation, the electrons can quickly reach a thermal equilibrium with ions (Fox & Loeb 1997, post-verified in our calculations). We thus adopt $T_e = T$ in our calculations.

3.2. Non-equilibrium Ionization (NEI) Model

In nature, if the plasma experiences shock, rapid dynamical processes (e.g., expansion, heating/cooling), the plasma may deviate from the CIE state, and enter into the so-called non-equilibrium ionization state (NEI, e.g., Dopita et al. 2002). Below we provide a brief description of the necessity of dealing with the NEI state. The basic equation to describe the ionization state is (Dopita et al. 2002):

$$\frac{1}{n_e}\frac{dF_z}{dt} = S_{z-1}(T_e)F_{z-1} - (S_z(T_e) + \alpha_z(T_e))F_z + \alpha_{z+1}(T_e)F_{z+1}, \tag{5}$$

where n_e is the electron number density, and $F_z = n_Z^z/n_Z$ is the ionic fraction of the zth ion, with $z = 0$ the neutral case and $z = Z$ the fully stripped ion of atomic number Z. The total number density of ion Z is $n_Z = \sum_{z=0}^{Z} n_Z^z$. $S_z(T_e)$ is the total

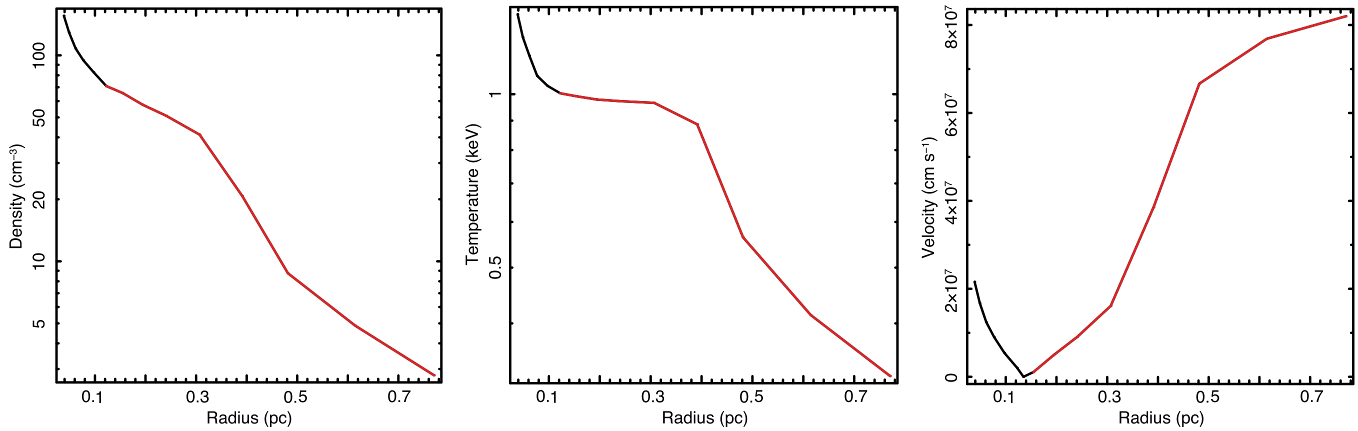

Figure 4. Electron number density ρ/m_p (left panel), temperature T (middle panel) and radial velocity $\boldsymbol{v}$ (right panel) of the diffuse circum-nuclear gas around Sgr A*, derived based on the inflow–outflow model. In each panel, black and red curves represent, respectively, the inflow and the outer regime. The stagnation point locates at $R \approx 0.14$ pc. Note that for Sgr A*, 0.1 pc $\approx 2\farcs5$.

ionization rate of transition from state z to state $z+1$ including the collisional ionization, autoionization, as well as the photoionization one; while $\alpha_z(T_e)$ is the total recombination rate of transition $z \rightarrow z-1$, which includes the radiative/di-electronic and charge transfer recombination.

When the left side of the above equation achieves zero, the ion ionization state does not change with time, i.e., the collisional ionization equilibrium. Because the coefficients of the ionization and recombination rate are both a function of the electron temperature T_e, the ionic fraction of each ion in the equilibrium state is coupled to T_e.

More generally, when the ionic state deviates from the equilibrium case, e.g., due to the variation of the electron temperature or the enrollment of extra medium, the ionization distribution of the ion changes with time according to Equation (5). It is apparent that the combination of two physical quantities in the denominator on the left side of Equation (5), $n_e \cdot \Delta t$, is the key parameter that determines the evolution of the ionization state, and it is defined as the ionization timescale τ in NEI calculations. The time-dependent change of ionization state should draw special attention when τ is longer than the timescale of kinetic cooling, as what happens in Sgr A*.

The key to dealing with NEI is calculating the ionization population of an atom fast and efficiently. To achieve that, ordinary differential equation and eigenvalue methods have been employed (Hughes & Helfand 1985; Smith & Hughes 2010) and integrated into the Python module `PyAtomDB`[13](Foster & Heuer 2020), as well as deriving the outcome spectrum after determining the ionization distribution. All kinds of radiation mechanisms (e.g., recombination, two-photon transition, bremsstrahlung) have been included during this procedure (Smith et al. 2001).

Figure 5 shows several example spectra of theoretical flux intensity. In these calculations, we assume the plasma consists of only oxygen, neon and iron, and the gas temperature is set to 1.5 keV. The ionization timescale of plasma is fixed to $10^{10}\,\mathrm{cm}^{-3}$ s. From bottom to top, four initial states are considered, (1) CIE state (assumed in most previous work); (2) all outer electrons of the plasma have been ionized; (3) all elements are not ionized at all; (4) the ions are ionized to be hydrogen-like. The left panel shows emission lines of oxygen and neon, and the right panel shows those of iron. In both panels, significant differences in emission lines between NEI and CIE are observed, suggesting that the potential capability of identifying NEI state when high S/N spectral data are available. In this work, we focus on the iron emission lines.

3.2.1. Timescale Estimations in an NEI System

Before detailed calculations of our model based on NEI, we here provide a rough estimation on two most important timescales, i.e., the dynamic timescale and the ionization timescale,[14] to decide if the plasma has reached the ionization equilibrium state. Here the dynamic (cooling) timescale is defined as $\tau_{\mathrm{dyn,cool}} = 1/(\boldsymbol{v}\, d\ln T/dr)$ (Ji et al. 2006), and the ionization timescale τ_{ion} can be determined from Equation (5).

Based on the CIE assumption, we then calculate the two timescales for the inflow–outflow diffuse plasma solution (shown in Figure 4), and the results are shown in Figure 6. In this plot, the solid curve represents $\tau_{\mathrm{dyn,cool}}$, while the ionization timescale of different iron ion species is shown by thin curves. The ionization degree of each iron ion decreases in

[13] https://atomdb.readthedocs.io

[14] Note that in the ionization balance process, generally speaking, the recombination timescale is much shorter than the ionization timescale.

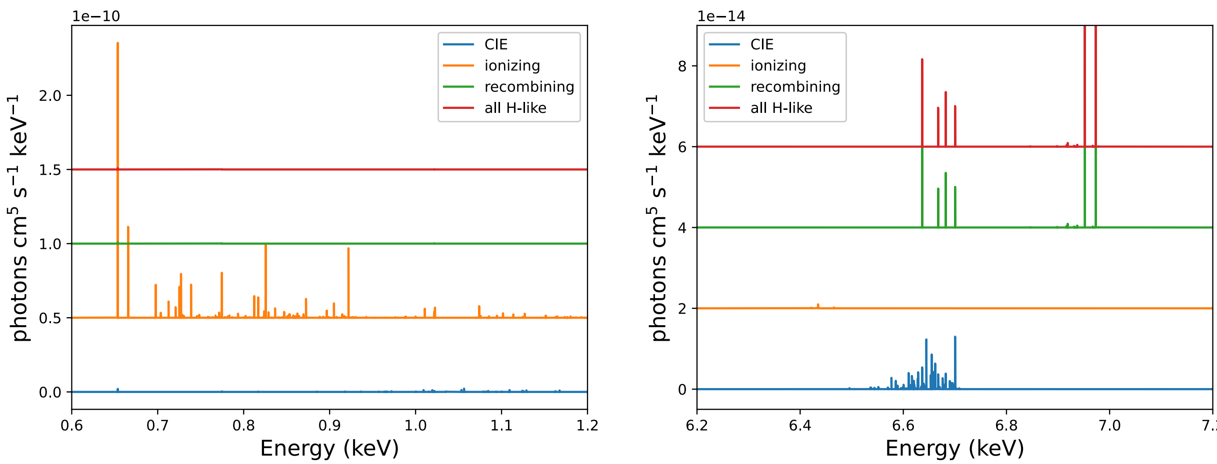

Figure 5. X-ray flux intensity of a plasma that consists only of oxygen, neon (left panel) and iron (right panel). The gas temperature and the ionization timescale are fixed to, respectively, 1.5 keV, and 10^{10} cm^{-3} s. From bottom to top, four initial states are considered: (1) CIE state; (2) all outer electrons of the plasma have been ionized; (3) all elements are not ionized at all; (4) the ions are ionized to be hydrogen-like. The intensities of the latter three are shifted for clarity.

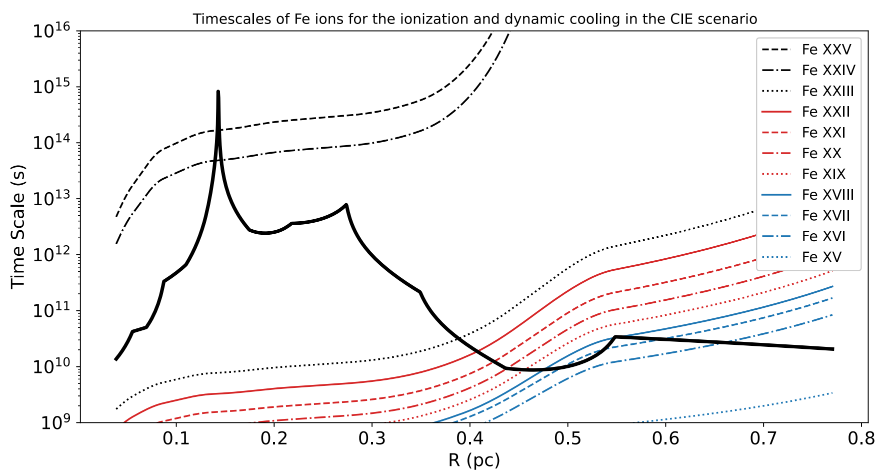

Figure 6. Dynamic (cooling) timescale ($\tau_{\rm dyn,cool} = 1/(v\ d\ln T/dr)$, shown by thick solid curve) and ionization/recombination timescale $\tau_{\rm ion}$ for each iron ion species (shown by thin curves) under the CIE assumption. The dynamic structure is based on an inflow–outflow solution (see Section 3.1 for details). The ionization fraction of each iron ion decreases from upper left (e.g., Fe XXVI and Fe XXV) to lower right. Clearly, outside of a certain radius ($\sim$0.4 pc, or equivalently, $\sim10''$), the recombination timescale (of certain ions) is longer than the dynamic cooling timescale, because of the decrease in gas temperature.

a direction from upper left to the lower right. As shown in this plot, we find that, inside of $\sim$0.4 pc (or equivalently, $\sim10''$), the recombination timescale of most ion species is much shorter than $\tau_{\rm dyn,\ cool}$. This suggests that, for most previous works that are only interested in $R \lesssim 10''$ (e.g., Xu et al. 2006), it is justified to take the CIE assumption.

On the other hand, as shown in Figure 4, gas outside of $\sim$0.4 pc ($\approx10''$) has a large radial velocity (up to $\sim6-8\times10^7$ cm s^{-1}) and a quick decrease in its temperature (down to $kT_e \sim$ 0.3–0.6 keV). The decrease in gas temperature is primarily because in our model this region no heating from shocks of stellar winds, see Section 3.1 and Equation (3). All these lead to a much shorter dynamic timescale $\tau_{\rm dyn,cool}$. Consequently, as shown in Figure 6, we will observe that the $\tau_{\rm ion}$ will exceed $\tau_{\rm dyn,cool}$. The CIE state cannot be reached in this region.

3.3. Projected X-Ray Emission

Considering the size of the emission region to be studied, the X-ray luminosity at frequency ν emitted by a spherically symmetric source within the range of R:

$$L_\nu = \int_R 4\pi r^2 n_e(r) n_{\rm H}(r) \Lambda_\nu(r) dr, \tag{6}$$

where Λ_ν is the emissivity at frequency ν, $n_{\rm e}$ and $n_{\rm H}$ are the densities of electrons and hydrogen atoms. We note that, the

X-ray continuum is the bremsstrahlung radiation from hot electrons.

Due to the projection effect in the actual observation, for a spherically symmetric system that is optically thin in X-rays, the flux at the ν frequency from a region between the projection radii of R_1 and R_2 is (Ji et al. 2006):

$$S_\nu(R_1, R_2) = \frac{1}{4\pi D^2}\int_{R_1}^{R_2} 2\pi R dR \times \int_R^\infty \frac{2r\, n_e(r) n_{\rm H}(r)\Lambda_\nu(r)}{\sqrt{r^2 - R^2}} dr, \tag{7}$$

where D is the distance from the source to us.

In practice, we also need to consider the instrumental response. The surface brightness of the source can then be expressed as (Ji et al. 2006):

$$\Sigma_X(R) = \frac{1}{4\pi}\int_R^\infty \frac{2r\, n_e(r) n_{\rm H}(r)}{\sqrt{r^2 - R^2}} \times \int_X \int_{X'} \Lambda_{\nu'} A(\nu') E(\nu', \nu) d\nu' d\nu dr, \tag{8}$$

where $A(\nu')$ is the effective area (Auxiliary Response File, ARF) at frequency ν', and $E(\nu', \nu)$ is the energy redistribution matrix (Redistribution Matrix File, RMF) between ν and ν'.

4. Results

4.1. Ionization Distribution

The dynamical structure of gas from $1''$ to $20''$ has been derived based on the inflow–outflow model (Shcherbakov & Baganoff 2010). Now we use this dynamical structure to derive the ionization distribution of oxygen and iron, the two most abundant metals. Technically, we assume all the gas moves from the stagnation point $R_{\rm st}$, where as suggested by Figure 6 we further assume the gas remains neutral. Actually, the initial ionization state has negligible impact on our calculations, the gas around the stagnation point will soon archive CIE state, since $\tau_{\rm dyn,cool} \gg \tau_{\rm ion}$, see Figure 6. Then, we follow the motions (either inward or outward) of the gas. The evolution time t of each grid is calculated by its grid size and the gas velocity of the dynamical model, and through Equation (5) we evaluate their ionization evolution at each radius. In order to increase the accuracy and promise convergence, we divide, at equal spacing in logarithmic scale, the whole computational regime into 1000 grids. The ionization/recombination rates in Equation (5) are loaded from the latest atomic database[15] and the calculations are performed by `PyAtomDB`.

Figure 7 shows the ionization distribution of oxygen (top panels) and iron (bottom panels) of the diffuse circum-nuclear gas around Sgr A*. For comparison purpose, we show in the left panels calculations based on CIE, and in the right panels calculations based on NEI. Several results can be observed immediately. First, the gas temperature is high enough that oxygen is almost fully ionized. O VIII contributes 1%–10% in most regions, and the fraction increases at larger radii. Consequently, there is in general no significant difference in ionization fraction between CIE and NEI for oxygen.

Now we focus on the iron case. We first note that, the irons remain weakly ionized. As shown in Figure 6, for given metal, the ionization timescale increases with increasing z. This is totally expected, since ionizing to z level means one further level ionization compared to the $z-1$ level. Inside the radius of $\sim$0.4 pc, the system remains in the CIE state (see also Figure 6), and the NEI scenario will have the same result to that of CIE. Outside of this radius, dramatic differences are observed. NEI processes lead to an increase of the ionization fraction for high-z (i.e., whose $z-1$ electrons are ionized) elements, and a decrease of the fraction for low-z elements. To summarize, we should expect to observe, in case of NEI, more high-z/Z metal elements located distant away from BH.

4.2. Theoretically Predicted Spectra (Intensities) at Different Locations

For a given ionization state and determined dynamical properties, theoretically the emission from each grid (i.e., nearly equivalent to that at a given radius R) can be derived in PyAtomDB.

Figure 8 shows the intensities between $0.5-9$ keV. Four radii are chosen as representatives, i.e., $R = 1\farcs3$ (top left), $R = 4\farcs0$ (top right), $R = 12\farcs0$ (bottom left), and $R = 18\farcs3$ (bottom right). We note that, the thermal broadening was not included in all these calculations. For consistency, all the calculations are based on the NEI model. As emphasized in previous sections, the top two panels are actually in CIE, while the bottom two panels are actually in NEI.

From this plot, we find that the differences between NEI and CIE are evident, especially at the $6-8$ keV band where iron lines are prominent.

4.3. Projected Spectrum from Selected Regions

We are now ready to calculate the projected spectra from specified/selected regions. In order to be consistent with our X-ray data analysis, we consider two regions, one is located between $2''$ and $5''$, and the other is located between $8''$ and $18''$. For our theoretical model, the outer boundary is limited to 1 pc ($\approx 25'' \approx 25\, R_{\rm bondi}$), outside of which we assume there is no X-ray emission and absorption. For the real nuclear environment of Sgr A*, we note that there exists a circum-nuclear disk at $R \sim 1-4$ pc (Genzel et al. 2010), the 1D model adopted here cannot remain valid in these regions.

Blue curves of Figure 9 show the intrinsic theoretical spectra of diffuse radiation from annular regions of the X-ray image, projected between $2''$ and $5''$ (inner region, shown in the left

[15] http://www.atomdb.org/

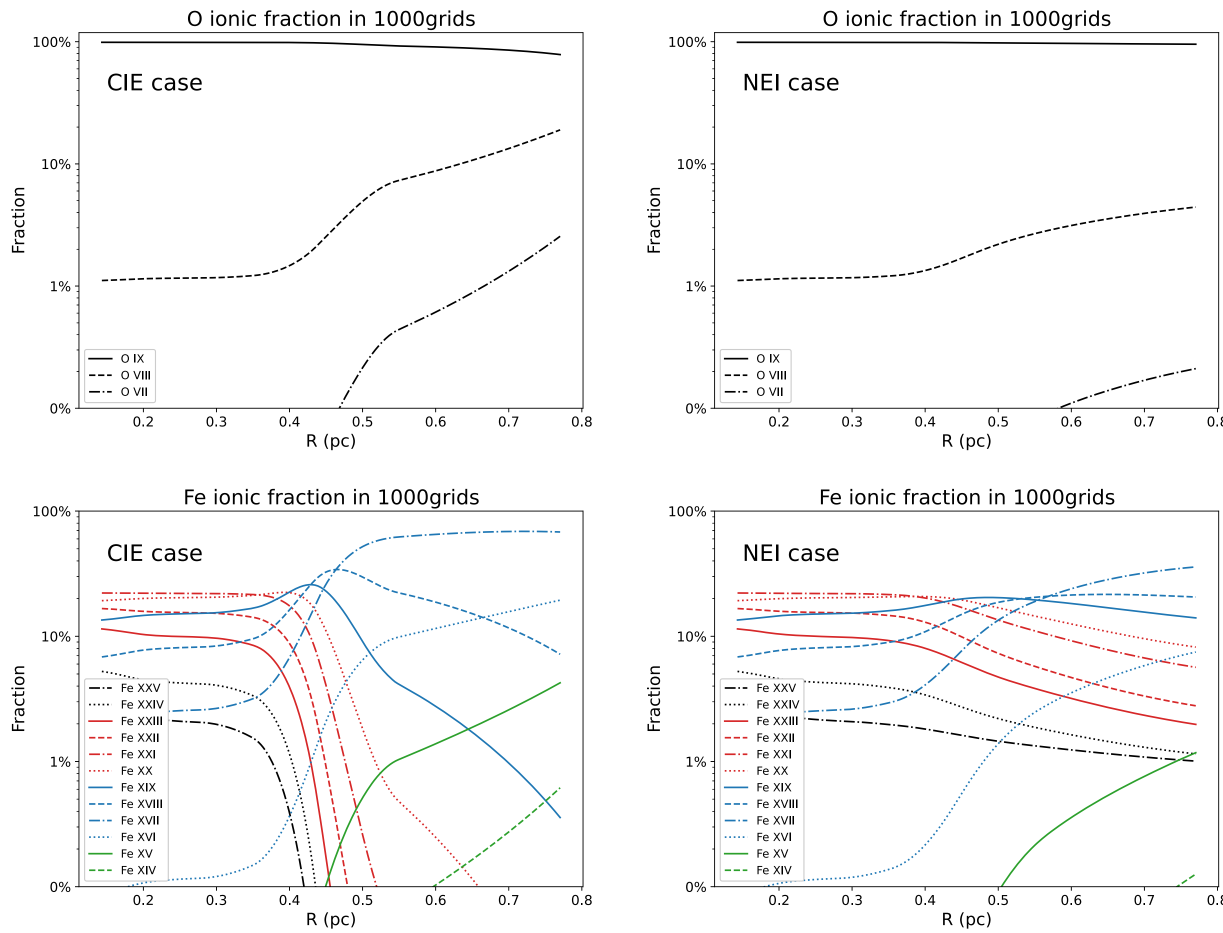

Figure 7. Ionization distribution of oxygen (top panels) and iron (bottom panels) of the diffuse gas. Left panels are calculated based on the CIE model, and right panels are based on the NEI model. In each panel, the ionized ion of each curve is labeled.

panel) and between 8″ and 18″ (outer region, shown in the right panel). In our calculations, neither absorption nor dust scattering of the foreground is considered. The results are shown in blue curves.

Apparently, the continuum is determined by gas density and temperature, thus we should not expect to observe any significant differences from the continuum emission. On the other hand, it is possible to identify NEI from CIE based on emission lines, which directly relate to the ionization state of each element species. For comparison, orange curves in both panels of Figure 9, where the fluxes are reduced by a factor of 10, show the results based on the CIE model. For the inner region, the spectrum of NEI is the same as that of CIE, as expected. On the other hand, for the outer region, some differences are observed, e.g., the soft $\lesssim$1 keV X-ray band (especially below ∼0.5 keV), and the 7.8 keV Kβ line of high-ionized iron (Phillips 2008).

The above theoretical spectral data sets are then loaded in ISIS. We note that, possible deviations to CIE below ∼0.5 keV and near 7.8 keV are unfortunately close to the energy boundaries of Chandra CCD detector, where the effective area in these bands are sufficiently low to have enough counts based on existing data, see also Figure 3. Moreover, extracting intrinsic X-rays below 2 keV also suffers large uncertainties introduced by dust scattering and foreground absorption. Below we only focus on the iron emission lines around 6.6 keV. We rebined the theoretical spectra to the energy resolution of Chandra, and the results are shown in Figure 10.

As shown in Figure 10, the line center and equivalent width of the ∼6.6 keV iron lines are, respectively, $\epsilon_{\rm c} = 6.62^{+0.02}_{-0.04}$ keV and $\mathrm{EW} = 595.7^{+219.6}_{-214.3}$ eV, based on a simple `Gaussian` model and assuming the exposure time is 10 Ms. For comparison, we also took similar procedures except for deriving the ionization state based on the CIE assumption to calculate the CIE results. This is shown by the blue solid curve in the plot. From a simple `Gaussian` fitting, the corresponding line center and equivalent width of the iron line are

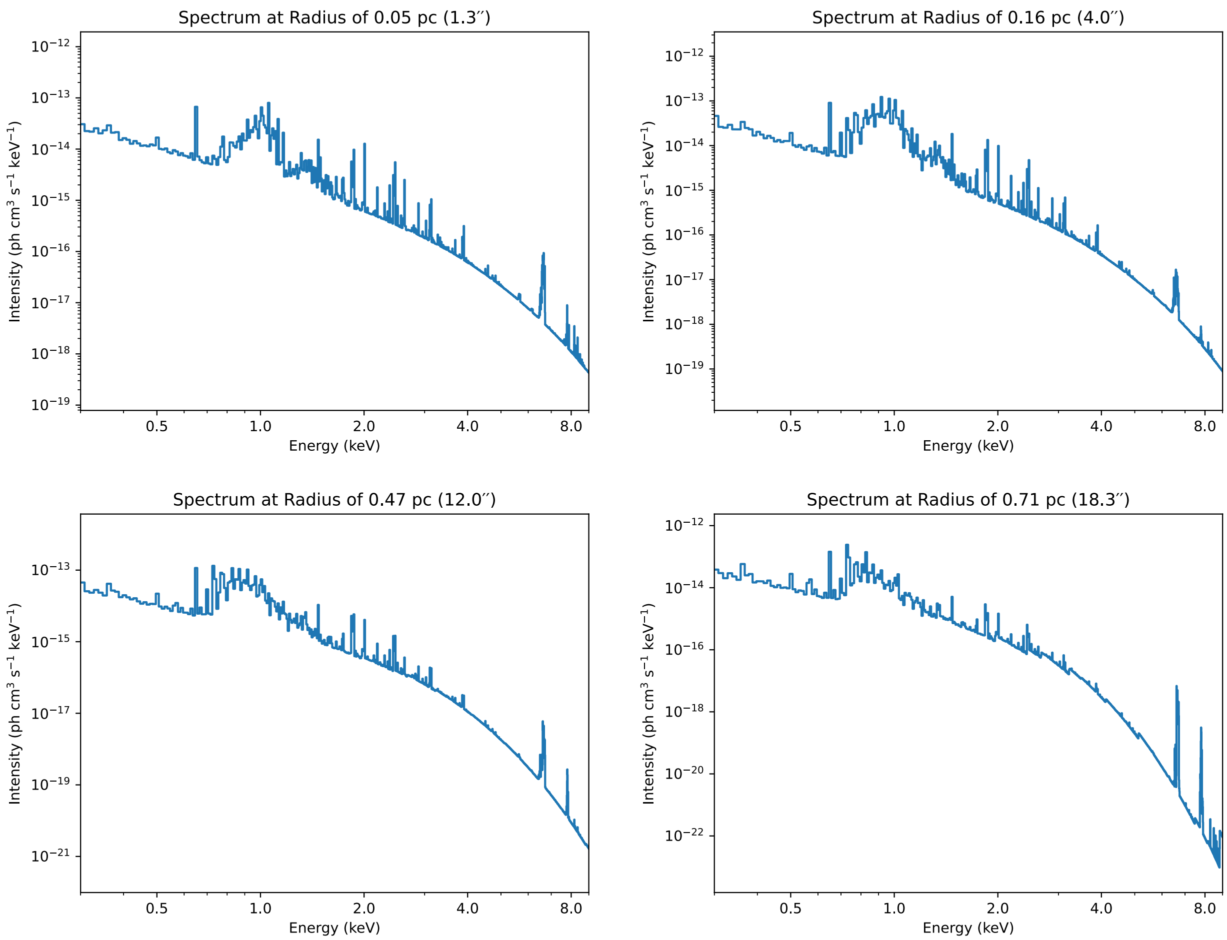

Figure 8. Theoretical spectra (actually emissivity) calculated for grids at different radii. The location of each calculation is labeled on top of each panel. For consistency, all the calculations are based on the NEI model, but the top two panels have already reached the CIE state, while the bottom two panels are actually NEI cases.

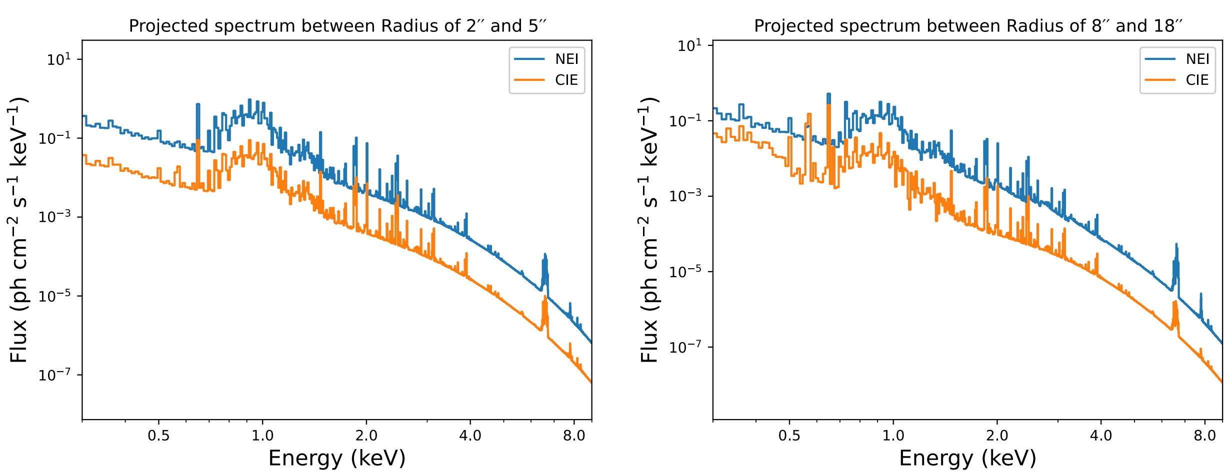

Figure 9. The theoretical, projected, spectrum from between 2″ and 5″ (left panel) and 8″–18″ (right panel). The dynamical structure of the inflow–outflow model is adopted. In both panels, results based on the NEI model (for radiation calculations) are shown in blue. For comparison, the orange curves in both panels show the results based on the CIE model, and the fluxes are reduced by a factor of 10 for clarity.

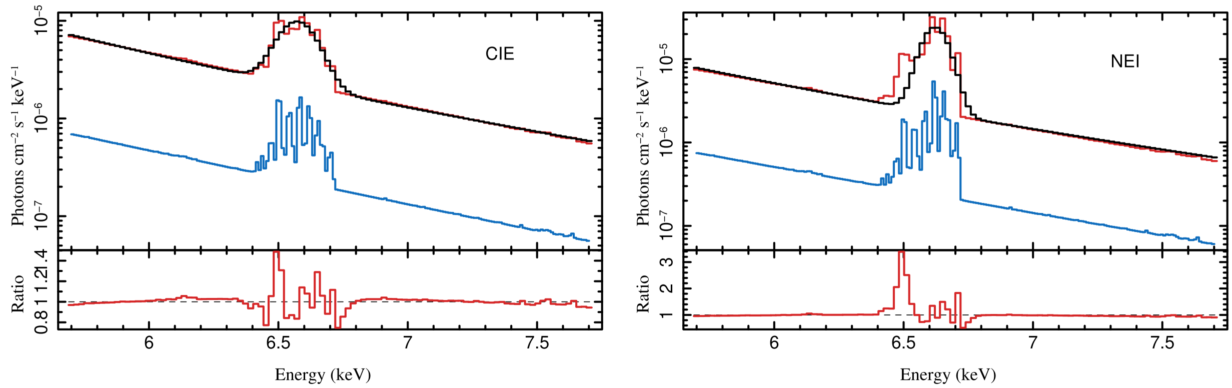

Figure 10. The iron emission line from a diffuse region (8″–18″) of Sgr A*. The blue line represents the original theoretically calculated spectrum (shifted down by a factor of 10). It is further rebined by the energy resolution of Chandra, which is shown by the red solid line. The black line shows the model under `powerlaw + Gaussian`. The model-to-input ratio is shown in the bottom panel.

respectively, $\epsilon_c = 6.57^{+0.05}_{-0.05}$ keV and EW = $419.4^{+192.4}_{-182.3}$ eV. This reflects the differences in ionization distribution between NEI and CIE at the 8″–18″ region. As shown in Figure 6, there will be more high ionization-state irons for the NEI case (compared to that for the CIE case). These high-z irons will intrinsically emit high-ϵ_c photons. Moreover, because of larger fraction of ionized irons, the intensity of emission lines will also be stronger, equivalently higher EW.

5. Summary and Discussions

Gases in the circum-nuclear regions, i.e., outside of the Bondi radius, are of crucial importance in studies of feeding and feedback of accretion onto supermassive BH (Quataert 2004; Genzel et al. 2010; Ressler et al. 2018). Besides, this is also the region where stellar winds, supernovae explosions and X-ray binaries may start to play important roles in shaping the gas dynamics.

In this work, we gather the largest Chandra data of Sgr A* to date, and extend the investigation from a near-Bondi region (i.e., 2″–5″, up to $\lesssim$10″, e.g., Quataert 2004; Xu et al. 2006; Shcherbakov & Baganoff 2010) to a further sub-pc distance (i.e., $\lesssim$20″), where winds from massive Wolf–Rayet and giant stars still dominate, in a collective way, the gas supply in this distant region (Cuadra et al. 2006; Martins et al. 2007; Ressler et al. 2018, 2023). This has now become possible, after the long-term efforts of Chandra projects devoted to Sgr A*. The exposure time of our final edited/cleaned data reaches ∼4.7 Ms, i.e., 1.39 Ms for ChI mode, 2.81 Ms for ChH mode, and 0.49 Ms for ChS mode. The S/N of the spectrum is now improved by a factor of ∼4 compared to previous works (e.g., Xu et al. 2006; Shcherbakov & Baganoff 2010).

With these updates (further distance from central supermassive BH, and higher S/N), we try to probe the possible observational evidence of NEI, which unlike CIE is a general state of ionization balance. Indeed, as summarized in Genzel et al. (2010), there are several hot ionized clumpy streamers or filaments that can penetrate deep into the central several arcseconds from Sgr A*. Motions by these streamers may introduce collisions with surrounding gas. Moreover, the possible X-ray ridge feature located in the outer region of this work (Rockefeller et al. 2005) suggest that there undergoes a supernovae explosion within past 2000 yr (see Zhang et al. 2023, not taken into account in this work). Consequently, gases in this region are promising to remain in an NEI state.

For comparison purpose, we consider two projected annuli, i.e., 2″–5″ for the inner region, and 8″–18″ for the outer region. In our investigation, the dynamical structure follows the inflow–outflow model (Quataert 2004; Shcherbakov & Baganoff 2010). In other words, the bremsstrahlung continuum in X-rays is fixed in our model. Our main results based on a detailed analysis of iron lines can be summarized as follows.

1. Observations of the inner regions of the diffuse X-ray emission reveal that, the iron line center locates at $\epsilon_c = 6.60^{+0.05}_{-0.03}$ keV. This is consistent with core emission of Sgr A* (Baganoff et al. 2003; Wang et al. 2013) and our theoretical modeling of this region based on NEI models, where we find that this region remains in the CIE case. On the other hand, the observed line strength (EW = $279.5^{+206.5}_{-134.4}$ eV) is weaker (by a factor of ∼2) compared to that derived from theoretical models (EW = $542.6^{+124.8}_{-123.1}$ eV).
2. Observations of the outer regions of the diffuse X-ray emission reveal that, the iron line center is located at $\epsilon_c = 6.65^{+0.02}_{-0.03}$ keV and the line strength is EW = $293.4^{+149.6}_{-149.6}$ eV. On the other hand, theoretical radiation calculations based on CIE and NEI models prefer, respectively, $\epsilon_c = 6.57^{+0.05}_{-0.05}$ keV and EW = $419.4^{+192.4}_{-182.3}$ eV, and $\epsilon_c = 6.62^{+0.02}_{-0.04}$ keV and EW = $595.7^{+219.6}_{-214.3}$ eV. Considering the uncertainties of observational data, we argue that the NEI model agrees with the observation better than the

CIE model on ϵ_c. However, both NEI and CIE predicts higher line strength (in form of a larger EW) than observed.

One problem of this work is that, the iron line strength (in the form of EW) predicted by our inflow–outflow model, exceeds the value constrained by observations. Below we highlight two caveats that may solve this issue.

First, and most plausible, is that the metal abundance may be different from our choice. In this work, we fix the abundance of the gas outside of the Bondi radius to 1.5, a mean value from modeling core (inside of the Bondi radius) emission from Sgr A* (Wang et al. 2013). However, the abundance is not firmly determined, i.e., $1.5^{+0.6}_{-0.4}$ (Wang et al. 2013), and its value may vary in different regions around Sgr A* (Hua et al. 2023). Clearly, the line strength is directly proportional to the metallicity of the gas, and a lower value (still consistent with that of Wang et al. 2013) will ease the over-predicted EW problem. Second, the gas dynamics may be oversimplified. Our model assumes a spherically symmetric geometry. However, as emphasized in Genzel et al. (2010), there are several hot ionized clumpy streamers or filaments within the central several arcseconds. These dense gas filaments will reduce the line strength of irons. Besides, the dynamical inflow–outflow model only considered wind supply within 10″. Although this is sufficient for investigating the feeding of Sgr A*, additional gas supplies from giant stars from i.e., 10″–50″ may be necessary. Third, Chandra observations of Sgr A* confirm strong wind/outflow that launches from hot accretion flow inside the Bondi radius (e.g., Wang et al. 2013). These hot gases can propagate to a larger region as probed in this work, and interact with interstellar medium there. This effect is also not included in our current model.

With the future X-ray mission, e.g., the Japanese XRISM (the X-Ray Imaging and Spectroscopy Mission) that covers the 0.3–12 keV band, the spectroscopic resolution (typically ∼5–7 eV) is high enough to resolve individual iron emission lines with microcalorimeters (XRISM Science Team 2020). The ionization state of the diffuse emission can then be determined, a crucial step in constraining the physical properties of the NEI state. Moreover, it can also provide constraints on the 7.8 keV Kβ line feature of high-ionized irons, which is missed by current Chandra observations due to low effective area (or equivalently, low S/N). This line, emitted by irons at higher ionization state, cannot be realized under the CIE scenario.

Acknowledgments

F.G.X. is supported in part by the National SKA Program of China (No. 2020SKA0110102), the National Natural Science Foundation of China (NSFC, Nos. 12192220 and 12192223), and the Youth Innovation Promotion Association of CAS (Y202064).

ORCID iDs

Shu Niu https://orcid.org/0000-0002-9930-5941
Fu-Guo Xie https://orcid.org/0000-0001-9969-2091
Wei Sun https://orcid.org/0000-0002-5456-0447

References

Aitken, D. K., Greaves, J., Chrysostomou, A., et al. 2000, ApJL, 534, L173
Baganoff, F. K., Maeda, Y., Morris, M., et al. 2003, ApJ, 591, 891
Borkowski, K. J., Sarazin, C. L., & Blondin, J. M. 1994, ApJ, 429, 710
Bower, G. C., Dexter, J., Asada, K., et al. 2019, ApJL, 881, L2
Bower, G. C., Wright, M. C. H., Falcke, H., & Backer, D. C. 2003, ApJ, 588, 331
Corrales, L., Baganoff, F. K., Wang, Q. D., et al. 2020, ApJ, 891, 71
Corrales, L. R., Mon, B., Haggard, D., et al. 2017, ApJ, 839, 76
Coti Zelati, F., Rea, N., Turolla, R., et al. 2017, MNRAS, 471, 1819
Cuadra, J., Nayakshin, S., & Martins, F. 2008, MNRAS, 383, 458
Cuadra, J., Nayakshin, S., Springel, V., & Di Matteo, T. 2006, MNRAS, 366, 358
Do, T., Hees, A., Ghez, A., et al. 2019, Sci, 365, 664
Dopita, M. A., Pereira, M., Kewley, L. J., & Capaccioli, M. 2002, ApJS, 143, 47
Event Horizon Telescope Collaboration, Akiyama, K., Alberdi, A., et al. 2022, ApJL, 930, L16
Foster, A. R., & Heuer, K. 2020, Atoms, 8, 49
Foster, A. R., Smith, R. K., & Brickhouse, N. S. 2017, in AIP Conf. Ser. 1811, Atomic Processes in Plasmas (APiP 2016) (Paris: AIP), 190005
Fox, D. C., & Loeb, A. 1997, ApJ, 491, 459
Genzel, R., Eisenhauer, F., & Gillessen, S. 2010, RvMP, 82, 3121
Gravity Collaboration, Abuter, R., Amorim, A., et al. 2019, A&A, 625, L10
Haggard, D., Nynka, M., Mon, B., et al. 2019, ApJ, 886, 96
Houck, J. C., & Denicola, L. A. 2000, in ASP Conf. Ser. 216, Astronomical Data Analysis Software and Systems IX, ed. N. Manset, C. Veillet, & D. Crabtree (San Francisco, CA: ASP), 591
Hua, Z., Li, Z., Zhang, M., Chen, Z., & Morris, M. R. 2023, MNRAS, 522, 635
Hughes, J. P., & Helfand, D. J. 1985, ApJ, 291, 544
Ji, L., Wang, Q. D., & Kwan, J. 2006, MNRAS, 372, 497
Kaspi, V. M., Archibald, R. F., Bhalerao, V., et al. 2014, ApJ, 786, 84
Lützgendorf, N., Helm, E. V. D., Pelupessy, F. I., & Portegies Zwart, S. 2016, MNRAS, 456, 3645
Ma, R.-Y., Roberts, S. R., Li, Y.-P., & Wang, Q. D. 2019, MNRAS, 483, 5614
Marrone, D. P., Moran, J. M., Zhao, J.-H., & Rao, R. 2006, ApJ, 640, 308
Martins, F., Genzel, R., Hillier, D. J., et al. 2007, A&A, 468, 233
Mossoux, E., Finociety, B., Beckers, J. M., & Vincent, F. H. 2020, A&A, 636, A25
Muno, M. P., Baganoff, F. K., Bautz, M. W., et al. 2004, ApJ, 613, 326
Narayan, R., Yi, I., & Mahadevan, R. 1995, Natur, 374, 623
Neilsen, J., Nowak, M. A., Gammie, C., et al. 2013, ApJ, 774, 42
Phillips, K. J. H. 2008, A&A, 490, 823
Ponti, G., De Marco, B., Morris, M. R., et al. 2015, MNRAS, 454, 1525
Ponti, G., Jin, C., De Marco, B., et al. 2016, MNRAS, 461, 2688
Quataert, E. 2002, ApJ, 575, 855
Quataert, E. 2004, ApJ, 613, 322
Rea, N., Coti Zelati, F., Viganò, D., et al. 2020, ApJ, 894, 159
Ressler, S. M., Quataert, E., & Stone, J. M. 2018, MNRAS, 478, 3544
Ressler, S. M., Quataert, E., & Stone, J. M. 2020, MNRAS, 492, 3272
Ressler, S. M., White, C. J., & Quataert, E. 2023, MNRAS, 521, 4277
Roberts, S. R., Jiang, Y.-F., Wang, Q. D., & Ostriker, J. P. 2017, MNRAS, 466, 1477
Rockefeller, G., Fryer, C. L., Baganoff, F. K., & Melia, F. 2005, ApJL, 635, L141
Scargle, J. D. 1998, ApJ, 504, 405
Scargle, J. D., Norris, J. P., Jackson, B., & Chiang, J. 2013, ApJ, 764, 167
Shakura, N. I., & Sunyaev, R. A. 1973, A&A, 24, 337
Shcherbakov, R. V., & Baganoff, F. K. 2010, ApJ, 716, 504
Smith, R. K., Brickhouse, N. S., Liedahl, D. A., & Raymond, J. C. 2001, ApJL, 556, L91

Smith, R. K., & Dwek, E. 1998, ApJ, 503, 831
Smith, R. K., & Hughes, J. P. 2010, ApJ, 718, 583
Smith, R. K., Valencic, L. A., & Corrales, L. 2016, ApJ, 818, 143
Spitzer, L. 1978, Physical Processes in the Interstellar Medium (New York: Wiley)
Wang, Q. D., Nowak, M. A., Markoff, S. B., et al. 2013, Sci, 341, 981
Wielgus, M., Marchili, N., Martí-Vidal, I., et al. 2022, ApJL, 930, L19
Wilms, J., Allen, A., & McCray, R. 2000, ApJ, 542, 914
Xie, F.-G., Narayan, R., & Yuan, F. 2023, ApJ, 942, 20
XRISM Science Team 2020, arXiv:2003.04962
Xu, Y.-D., Narayan, R., Quataert, E., Yuan, F., & Baganoff, F. K. 2006, ApJ, 640, 319
Yuan, F., & Narayan, R. 2014, ARA&A, 52, 529
Yuan, F., Quataert, E., & Narayan, R. 2003, ApJ, 598, 301
Yuan, Q., & Wang, Q. D. 2016, MNRAS, 456, 1438
Zhang, M., Li, Z., Hua, Z., & Morris, M. R. 2023, MNRAS, 522, 3568
Zhang, S., Baganoff, F. K., Ponti, G., et al. 2017, ApJ, 843, 96
Zhu, Z., Li, Z., & Morris, M. R. 2018, ApJS, 235, 26